Chapter 5

Shubnikov–de Haas oscillation and 3D Fermi surface topology of nodal line semimetal InBi

5.1 Introduction

Before introducing the experimental part, we have discussed the basic electronic structure of InBi. Our study suggest that only two bands contribute carrier's density at E_{F}. Energy dispersion of the band-1 and band-2 are shown in FIG. 5.1 where allowed electron and hole-like states are shown in red and blue shaded areas respectively. FIG. 5.1 indicates that γ and α-pockets coming from band-1 are electron types. Similarly, β and δ-pockets coming from band-2 are hole types. We have shown the 3D Fermi surface in FIG. 5.2. The FS coming out from the band-1 creates two distinct pockets γ and α placing at high symmetric points Z and R respectively. Similarly, the FS coming out from the band-2 creates two distinct pockets β and δ placing at high symmetric points Γ and M respectively.

After identifying all the electron and hole pockets, we have calculated the extremum area of these pockets. To draw the extrema, we take several cuts in $k_x - k_y$ plane in 3D BZ. The contours from several cut perpendicular to the k_z axis are shown in FIG. 5.3. The red

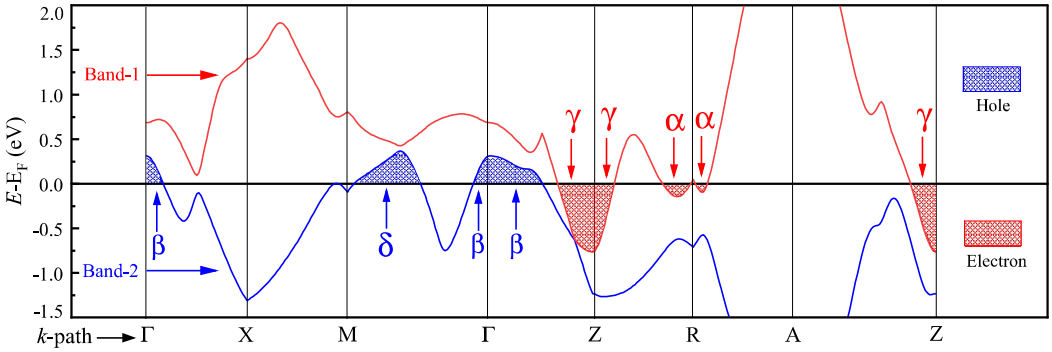

Figure 5.1: The bandstructure of the band-1 is shown in red. The allowed states marked by red shaded area denoted the electron-like pocket. The γ and α pockets are generated from the band-1. The bandstructure of the band-2 is shown in blue. The allowed states marked by blue shaded area denoted the hole-like pockets. The β and δ pockets are generated from the band-2.

and blue contours come from band-1 and band-2 respectively. FIG. 5.3 (b)-(e) suggests that the extremum area of β and δ sheets lie at the Γ point. The cut corresponding to the Γ point is shown in FIG. 5.3 (b) where maxima of the FS are indicated by a arrow. It is visible that the area of the β and δ sheets continuously decreases from CUT-1 to CUT-4. Similarly, from CUT-5 to CUT-8, the area of the γ and α sheets continuously increase. The maximum area of γ and α sheets lies at Z-point (CUT-8). The extremum area of γ and α-sheets are indicated by the arrow in FIG. 5.3 (i). The extremum area of all four FS is listed in TABLE-5.1.

5.2 Experimental verification

The quantum oscillation work of InBi was performed by Y. Saito[145] in 1964. In this same work, the author performed de Haas-van Alphen (dHvA) oscillation for InBi. After Saito's work, many authors performed the quantum oscillation study, but none of them successfully resolved the nature of electron and hole pocket from the oscillatory data. In 1973 Meyer *et al.*[121] performed dHvA study of InBi in all crystallographic directions. We have shown a part of Meyer's result in FIG. 5.5 as a reference. The author predicts that F_β and F_γ are originating from the InBi and F_δ is originating from the impurity band. Observing the angular variation of dHvA oscillation, Meyer *et al.* first predicted that the

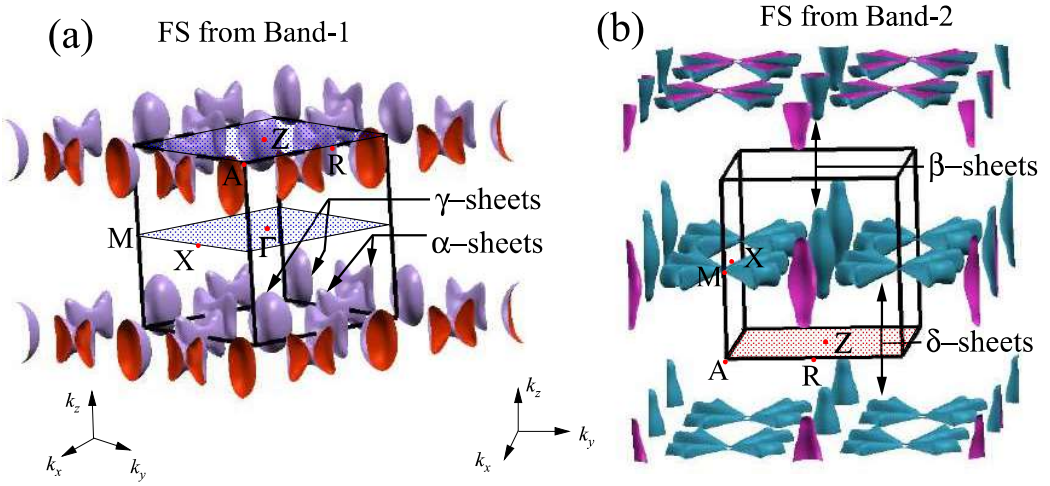

Figure 5.2: (a) The electron pockets come from band-1. The γ and α sheets are lying at high symmetric Z and R points respectively. (b) The hole pockets come from band-2. The β and δ sheets are lying at high symmetric Γ and M points respectively.

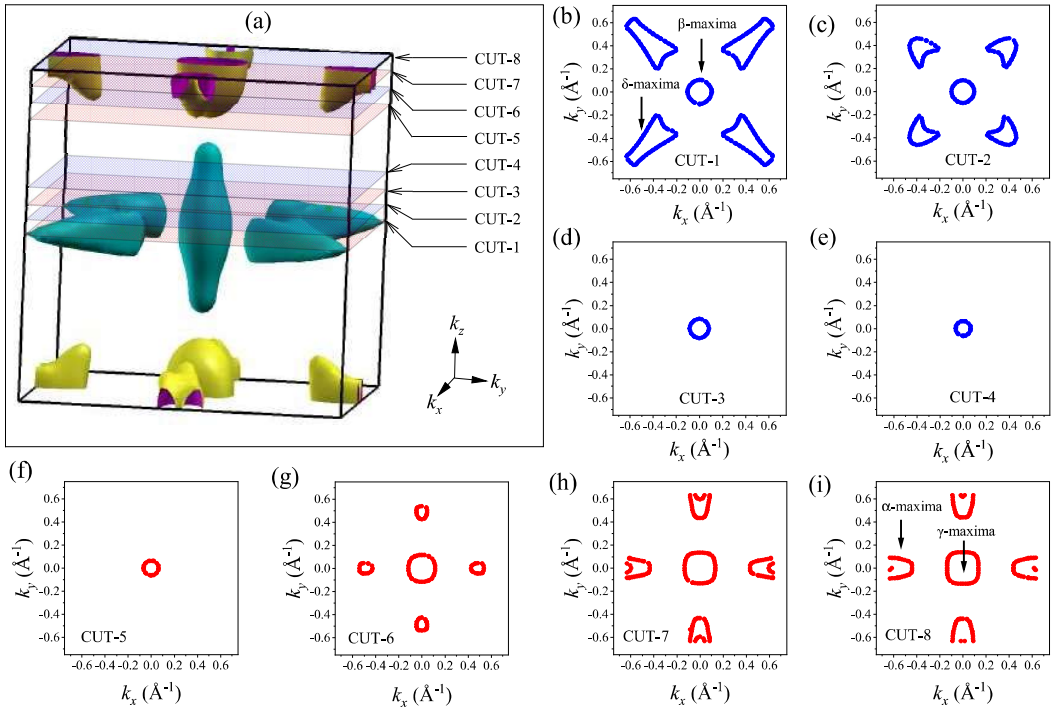

Figure 5.3: Fermi sheets in k_x-k_y plane at several k_z cut. (a) Several k_x-k_y plane in 3D BZ where the 2D contours are plotted. (b)-(d) The contours in blue coming from band-2. the areas of β and δ sheets are continuously decreasing from CUT-1 to CUT-4. The arrow mark in CUT-1 indicates the extremum area of the corresponding pockets. (f)-(i) The contours in red coming from band-1. the areas of α and γ sheets are continuously increasing from CUT-5 to CUT-8. The arrow mark in CUT-8 indicates the extremum area of the corresponding pockets.

3D topology of the FS originated from F_β and F_γ should be distorted ellipsoid. From the angle-dependent data, they cannot reveal the origin of each FS from the BZ structure. We brought the Meyer's result as it plays a crucial role in the context of our current study. We started our experiment with magneto-transport studies *viz.* MR at low temperature and high magnetic field. To get the SdH signal, we measured MR at 3 K, 5 K, 10 K, and 15 K in the **B**-field 7–15 T. The MR data and corresponding FFT spectrum are shown in FIG. 5.4 (b) and (a) respectively. To perform FFT, we first plot the resistivity as a function of the inverse magnetic field. Then we take the double derivative to subtract the background. The advantage of taking the double derivative is that it eliminates the background but retains all oscillatory components. We use this data as a time scale spectrum to perform the FFT. After identifying the frequency that comes from the Fermi surface of the compound, we take an inverse FFT for the particular frequency to visualize the time scale spectrum of the particular frequency component. The range of frequencies that are used to take the deconvolution are as follows; $F_\beta \rightarrow$ 316–341 T, $F_\delta \rightarrow$ 528–553 T and, $F_\gamma \rightarrow$ 780–804 T. The range is decided based on the width of the corresponding frequency peaks observed in the FFT spectrum (FIG. 5.4 (a)). A detailed discussion regarding the oscillatory data is put in the supplementary article[146] . All FFT peaks named as F_β, F_δ and F_γ are highlighted in FIG. 5.4 (a). The time scale spectrum for the corresponding frequency peaks is shown in FIG. 5.4 (c)-(e). The oscillations shown in the FIG. 5.4 (c)-(e) are the raw oscillations derived from the 3 K MR data. We observed a considerable amount of beat formation in the time scale spectrum. The formation of beats (originate from the frequency broading) in the oscillations is a common occurrence for any compound[147]. Regarding the FFT spectra (FIG. 5.4 (a)) of the compound, we observed many small peaks between 550 – 650 T, which might come from several factors. Peaks observed at higher temperatures are majorly contributed by thermal noise which is random in nature. The Small peaks (585 T and 660 T) observed at 3 K are interesting. The peak at 660 T is exactly double of F_β (330 T) which signifies that it is the harmonic of F_β. The peak at 585 T might originate from other factors *viz.* in-homogeneity of the sample, non-uniformity of the source magnetic field or spreading of crystal orientation (dislocation).

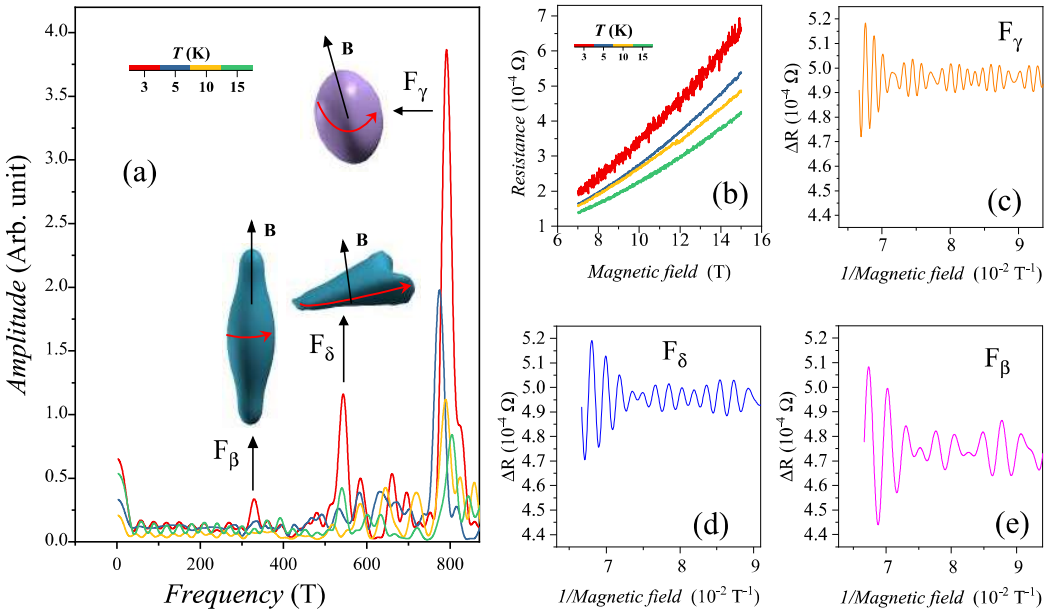

Figure 5.4: The FFT spectrum and SdH oscillation. (a) The FFT spectrum calculated at 7-15 T field from the second derivative of the MR data. The red arrow indicates the extremum orbits of the corresponding pockets from where frequency peaks are coming. (b) The actual MR data from where FFT is performed. (c)-(e) The deconvoluted spectrum coming from corresponding pocket at 3 K.

5.2.1 Frequency from β-sheets (F_β)

The F_β of FFT spectrum is observed at 330 T as shown in FIG. 5.4 (a). The extremum area of the corresponding FS is close to our theoretical calculation (see the TABLE-5.1). As shown in FIG. 5.6 (j), the 3D shape of β-pocket looks like a distorted ellipsoid structure. The angle dependent study of F_β by Meyer *et al.* is shown by a red dashed line in FIG.

Table 5.1: Fermi sheets properties

FS pocket	Origin	Type	Experimental SdH[a] Frequency (T)	Experimental area[b] (nm^{-2})	Theoretical area[(c)] (nm^{-2})
β	Band-2	Hole	330	3.1	3.4
δ	Band-2	Hole	543	5.1	5.3
α	Band-1	Electron	Merged with β	–	3.3
γ	Band-1	Eectron	792	7.5	6.7

(a) At 3 K and **B** along the *c*-axis, (b) Area derived from our SdH frequency
(c) Extremum area (from our DFT calculation) in k_x-k_y plane

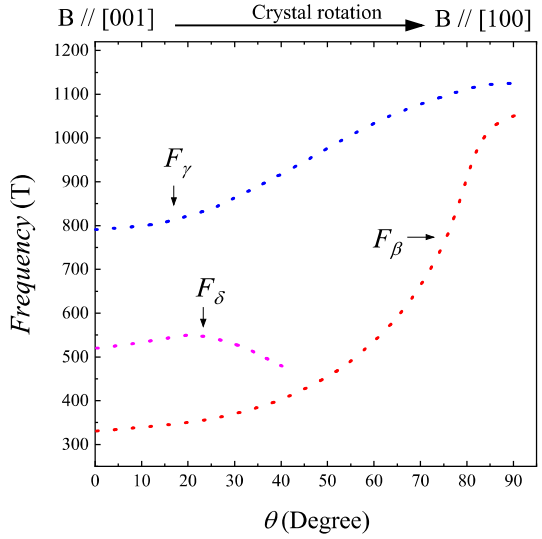

Figure 5.5: Data taken from Meyer *et al.*[121]. Angle dependent variation of three major frequencies F_β, F_γ and F_δ

5.5. It indicates that if we change the crystal orientation from [001] to [100], F_β changes from 330 T to 1052 T. The angular dependency of F_β suggests that the semi-major axis of the pocket is 3.3 times longer than its semi-minor axis. Such kind of experimental result is very consistent with our theoretically generated FS structure. Our theoretical calculation also suggests that if we move the E_F slightly upward (electron dope), the pocket size becomes lower. Our system might behave as an electron-doped compound, as it shows slightly lower FS area than the theoretical one.

5.2.2 Frequency from δ-sheets (F_δ)

The F_δ of the FFT spectrum is observed at 543 T as shown in FIG. 5.4 (a). Origin of the particular frequency was not established earlier. Our study suggests that the F_δ comes from the distorted triangular shape FS lying at the M point. This FS has a four-fold symmetry as shown in FIG. 5.6 (k)-(m). The FIG. 5.6 (l) indicates that at $E = E_\mathrm{F}$ the four petals are connected and electrons can move through the FS to make a complete loop. The extremum orbit of the electron path is marked by a red dashed line. There is an additional possibility that electrons can circulate within a single petal of FS as the linkage between two petals is infinitesimally small. Our study suggests that any finite upward movement of E_F can disconnect the linkage among the petals. We show an example in FIG. 5.6 (m)

where a 10 meV upward shift of E_F (electron-doped) breaks the connection among petals. As our system behaves as an electron-doped (as discussed earlier), we can easily assume that the four petals are disconnected from each other and electron move through the extremum orbit within a single petal as shown in FIG. 5.6 (m). The theoretically calculated extremum area of a single petal is very close to the experimental one which unambiguously supports the claim stated earlier. The DFT calculation slightly overestimates the FS area, indicating the electron-doped system.

The structure of the δ pockets in different angle are shown in FIG. 5.6 (c). Observing the 3D nature of the pockets we can say, area of the pocket in $k_x - k_y$ plane is much larger than the area along $k_x - k_y$ plane. Interestingly, F_δ from angle dependent dHvA changes according to this FS topology. The angular variation of F_δ is shown by the dashed magenta line in FIG. 5.5. The data suggest that when crystal lies in [001], F_δ has its highest value. But with the tilting towards [100], F_δ started to decrease. As the area of the pocket in $k_x - k_y$ is very small, no signal was observed along [100] direction. Such an angle dependent study again strongly verify the nature of the FS.

5.2.3 Frequency from α-sheets (F_α)

The frequency corresponding to the α sheet is not observed by us because the extremum area of the α and β sheets are very close to each other (see TABLE-5.1) and hence, both frequencies are superimposed to each other. We show how the FS evolves from hole-doping to electron-doping in FIG. 5.6 (g)-(i) for the completeness of our study. We observed that a 100 meV downward shift of E_F (hole doping) can break the α sheet into two equal parts. On the other hand 100 meV upward shift of E_F (electron doping) enhance the volume of the FS. The extremum orbit in the $k_x - k_y$ plane is indicated by the red arrow in FIG. 5.6 (h).

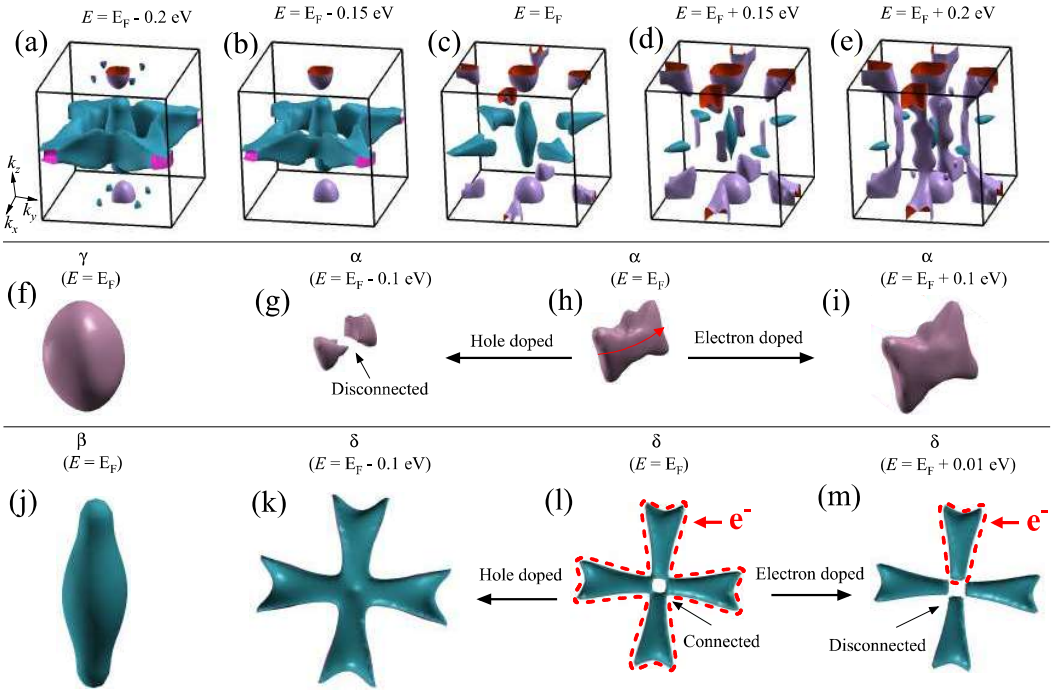

Figure 5.6: The veriation of FS from hole doping to electron doping. (a)-(e) The evolution of 3D BZ from hole doping to electron doping. (f) The shape of the γ pocket at E = E_F. (g)-(i) The evolution of α pocket from hole doped to electron doped. The extremum orbit parallel to k_x-k_y plane is shown by the red arrow. The substantial hole doping split the α pocket by two parts. (j) The shape of the β pocket at E = E_F. (k)-(m) The evolution of β pocket from hole doped to electron doped. The extremum orbit parallel to k_x-k_y plane is shown by red dotted line.

5.2.4 Frequency from γ-sheets (F_γ)

F_γ is observed at 792 T in the FFT spectrum as shown in FIG. 5.4 (a). The FS area corresponding to γ-sheets is the largest and most intense compared to all other pockets. The particular frequency comes from ellipsoid-shaped FS lying at the Z-point of the BZ. The 3D shape of the γ-pocket is shown in FIG. 5.6 (f) The angle dependent study of F_γ is shown by the blue dashed line in FIG. 5.5. It indicates that if we change the crystal orientation from [001] to [100], F_γ changes from 790 T to 1124 T. The angular dependency of F_γ suggests that the semi-major axis of the pocket is 1.5 times longer than its semi-minor axis. Such kind of experimental result is very consistent with our theoretically generated FS structure. Unlike the β and δ, experimental FS area of γ-pocket is slightly lower than the theoretically predicted one (see TABLE-5.1). Lowering the FS area of any electron pocket is justifiable for an electron-doped system. The amplitude of F_γ shows the adequate temperature dependency that help us to calculate the 'effective mass'. The parameters *viz.* 'effective mass' and 'Dingle temperature' derived from the F_γ are discussed in details in the subsequent section.

5.2.5 Temperature dependent raw oscillatory data at 3 K

The oscillatory component of the MR data at various temperatures are shown in FIG. 5.7 (a). The oscillatory components are derived from the 2^{nd} derivative of the raw MR data. One important feature of the oscillatory data is that it shows amplitude damping with the increasing inverse magnetic field proving the existence of quantum oscillations in our MR data. The temperature dependent time-scale spectra of F_γ (filtered at 740-860 T) is shown in FIG 5.7 (b). Both of these figures [FIG 5.7 (a)&(b)] indicate that amplitudes of the oscillations have been damped with the increase of temperature which is consistent with the quantum oscillatory phenomenon.

The detailed discussions regarding FFT and other parameters are put in the main manuscript. The raw resistance data and its oscillatory components originate from individual Fermi sheets are shown in FIG. 5.8. The amplitude of the resistance and the oscillatory data are

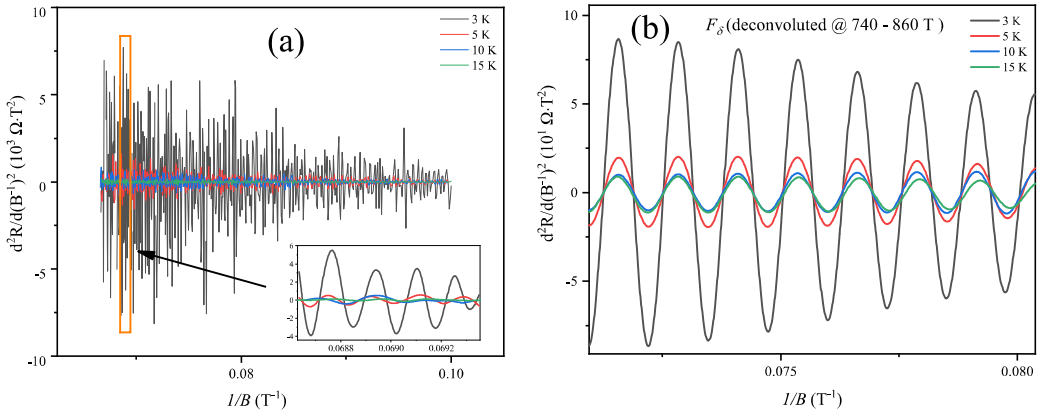

Figure 5.7: (a) Oscillatory components of the resistivity data (calculated from the 2^{nd} derivative) measured at several temperatures. (Inset) The enlarged view of data that lies within the orange colored rectangle. (b) The time scale spectra of F_γ derived at several temperatures.

kept in the same scale in FIG. 5.8. We observed that with the increase of the frequency the amplitude of the oscillations decreases. To get the F_γ, F_δ and F_β, inverse FFT is performed in the frequency range of 740-860 T, 506-559 T and 306-351 T. The range of the frequencies is chosen based on the width of the corresponding peak in FFT spectra (discussed in the main article).

Due to the 2^{nd} derivative, an additional multiplication factor (that is proportional to the frequency) is introduced with each sinusoidal component which further increases the amplitude of the high frequency components in the FFT spectra. So, unlike the raw data (FIG. 5.8), we observed ascending order of amplitude from F_β to F_γ in FIG. 11 (a). Such kind of amplitude modulation does not alter the physical parameters of the compound. A brief comparison between raw and 2^{nd} derivative data is discussed below.

A. Temperature-dependent amplitude: Temperature-dependent amplitude is derived from the F_γ frequency (discussed in the main article). A constant multiplication factor in amplitude is added in the 2^{nd} derivative data for F_γ. The constant multiplication factors are equal for all the temperature as the F_γ for all the temperatures remain same. Hence m^*, which is calculated from relative amplitude of the temperature-dependent F_γ, could not be altered at all.

B. Phase part of the oscillation: As we performed derivative two times, phase of the

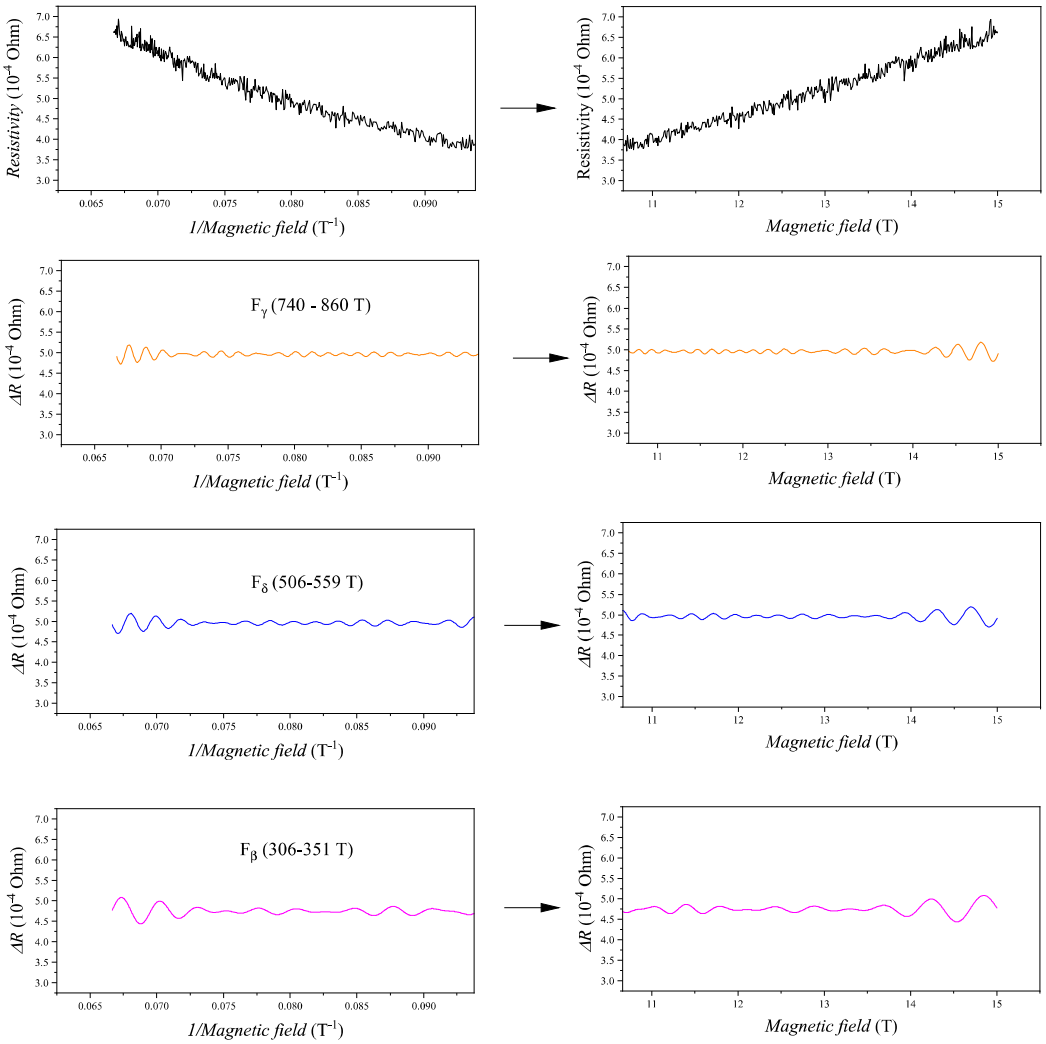

Figure 5.8: Raw oscillations originate from the corresponding Fermi sheet at 3 K. (Left panel) Actual resistance data and the oscillations originate from the particular Fermi sheet as a function of **inverse** magnetic field. (Right panel) Actual resistance data and the oscillations originate from the particular Fermi sheet as a function of magnetic field.

oscillation remain same for all of its sinusoidal components.

5.3 The study of effective mass and Dingle Temperature

The oscillation pattern of the resistivity is described by the Lifshitz-Kosevich (LK) formula

$$\Delta R \propto -B^{\lambda} R_T R_{\mathrm{D}} R_S \sin\left[2\pi\left(\frac{F}{B} - \Gamma - \Delta\right)\right] \tag{5.1}$$

Table 5.2: Parameters derived from the F_γ oscillation. m^*, effective mass; T_D, Dingle temperature; τ, relaxation time and μ_q, quantum mobility.

m^* (Units of m_0)	T_D (K)	τ (ps)	μ_q ($m^2V^{-1}s{-}1$)
0.40	1.1	1.2	0.53

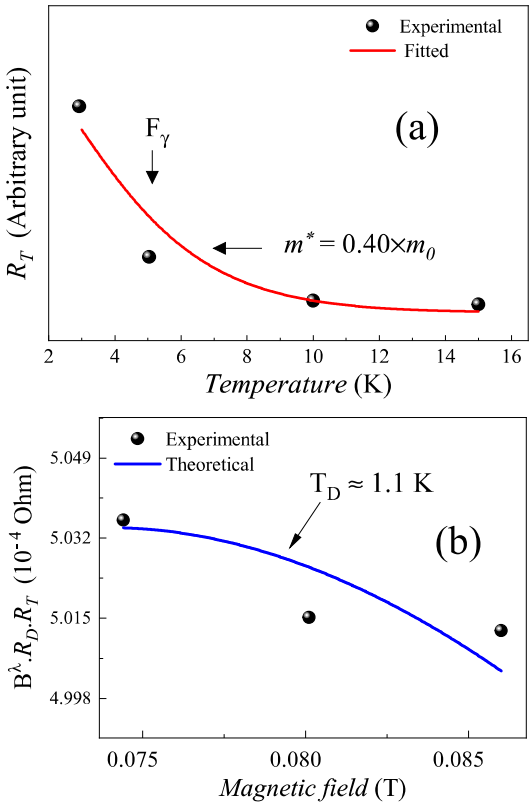

Figure 5.9: (a) Calculation of m^* from T-dependent amplitude of SdH oscillation. (b) The amplitude-simulation using L-K formula to derive T_D.

where $R_T = \alpha T\mu/B\sinh(\alpha T\mu)$, $R_D = \exp(-\alpha T_D\mu/B)$ and $R_S = \cos(\pi g\mu/2)$. μ is the ratio of the effective cyclotron mass m^* to free electron mass m_0. T_D is the Dingle temperature, and $\alpha = (2\pi^2 k_B m_0)/(\hbar e)$. The oscillation phase is described as a sine term with an additional phase factor $\Gamma - \Delta$, in which $\Gamma = \frac{1}{2}$ - $\phi_B/2\pi$ and ϕ_B is the Berry phase. The dimensionality of FS is determined by the phase shift Δ. For 2D FS, $\Delta = 0$. For 3D FS, Δ can take value $\pm$ 1/8 according to the minima and maxima of the FS area. The Berry phase in our case is not robust and hence we do not draw any conclusive remark regarding the topics. The unreliable Berry phase can originates from the insufficient maximum field in the quantum oscillation study[127]. The term λ is also determined by the

FS dimensionality. λ can takes value $\frac{1}{2}$ and 0 for 3D and 2D FS respectively. From the L-K formula, effective mass m^* can be calculated from the fit of the thermal damping factor R_T with the temperature dependence amplitude of the oscillation. From the SdH oscillation, we have observed that an adequate T-dependent signal comes only from F_γ. From the T-dependent amplitude-damping, we have calculated the effective mass (m^*) of the electron. The fitting of R_T for the F_γ is shown in FIG. 5.9 (a) The derived m^* from the calculation is approximately $0.40 \times m_0$. Putting the value of m^*, we have theoretically estimated the Dingle temperature (T_D). The amplitude of the oscillation with varying T_D is shown in FIG. 5.9 (b). Our estimated T_D from the fitted data is approximately 1.1 K. The Dingle temperature of the compound has a microscopic origin closely related to the carrier's scattering. Our low T_D indicates that sample has low imperfections *viz.* dislocations and mosaic structure[147].

Using Dingle temperature T_D ($\sim$ 1.1 K), we have calculated the quantum relaxation time $\tau_q = \overline{h}/2\pi k_B T_D = 1.20 \times 10^{-12} s$ and quantum mobility $\mu_q = e\tau_q/m^* = 0.53$ m^2 V^{-1} s^{-1}. All estimated parameters from the F_γ are listed in TABLE 5.2. The quantum mobility (μ_q) at 3 K is very close to the compound's effective mobility (μ_{eff}) estimated from Hall data at the same temperature. The consistent result suggests that our experimental outcome from SdH oscillation and the Hall measurement is very reliable. Our estimated quantum mobility is slightly lower than the classical mobility. Such a phenomenon is expected because quantum mobility is sensitive to both small-angle and large-angle scattering. On the other hand, classical Drude's mobility is only influenced by large-angle scattering[148].

5.4 Conclusion

We successfully resolved the 3D structure of every electron and hole pocket with the help of Shubnikov-de Haas oscillation. The SdH oscillations were found to be quite rich as most of the FS contributing to the oscillations. The quantum oscillation study also helped to estimate important parameters (effective mass and Dingle temperature) of InBi for the first time. Our study reveals that two bands, each electron and hole-like, majorly contribute

to transport phenomena. The holes contribute from one pocket lying at the central and four pockets lying at the corner of the BZ. Similarly, the electrons come from one pocket lying at the body center and four pockets at the edge of the BZ. The collective participation of each electron and hole pockets makes the compound nearly perfect compensated semi-metal at low temperature. The modulation of electron and hole pockets occurred as if the compound behaved slightly electron doped at 3 K. The structure of each Fermi sheets excellently matches with the theoretical result. The unique Fermi surface topology governing the carrier compensation is closely correlated to the magneto-transport phenomena of the compound.